RSC Advances

PAPER

View Article Online
View Journal | View Issue

Cite this: *RSC Adv.*, 2025, **15**, 26403

Design of a 3D-printing fluorescence detector for HPLC separation: a prototype device†

Xuewan Wu, Yanting Liu, Ziyi Xiao, Ruyi Deng, Rui Huang, Hongjun Luo* and Kaisong Yuan*

Received 2nd May 2025
Accepted 17th July 2025

DOI: 10.1039/d5ra03108g

rsc.li/rsc-advances

Herein, we developed a three-dimensional (3D)-printing fluorescence detector that could be connected to the HPLC system, and distinguished by its ease of assembly, cost-effectiveness, and high adaptability. The detector comprises a laser diode, a 3D-printing flow cell, quartz glass, a long-pass filter, a silicon phototube, and a voltmeter. Technically, the flow cell we designed here has a very compact structure, and it is convenient to embed the optical filter and the phototube, which is also a highlight of our detector to ensure the miniaturization of the whole device. Through the optimization of the detector's structural configuration, the adjustment of the various dimensions and relative positions of the detection window, and the removal of the metal encapsulation cover of the silicon phototransistor, we achieved the optimal detection sensitivity and stability. Experimental findings indicate that the 3D-printing fluorescence detector achieves a limit of detection (LOD) of 5 μg mL^{-1}, a linear detection range of 5–60 μg mL^{-1}, and exhibits reasonable inter-day and intra-day stability. Finally, the detector demonstrated its practical utility by successfully separating and detecting a mixed solution of rhodamine 6G and rhodamine B, underscoring its potential for real-world applications.

1. Introduction

The fluorescence detector is a common but critical instrument that has been widely coupled to different separation techniques such as High Performance Liquid Chromatography (HPLC) and Capillary Electrophoresis (CE), which show great importance in food, environment, or bioscience analysis.[1–3] Many commercialized fluorescence detectors have been developed and show high sensitivity, stability and accuracy for analytical purposes. There is no doubt that they hold an irreplaceable position in reliable detection. Yet, such instruments usually are bulky and expensive.[4] The development of home-made fluorescence detectors with miniature size, simple configuration and low-cost features make such instruments more accessible. Although their performance is not as good as that of commercialized ones, they can still play a certain role in situations where the detection requirements are relatively low. In certain specialized scenarios, such as spaceflight missions, the miniaturized design of the device also satisfies such requirements.[5]

The miniaturization of fluorescence detectors necessitates a compact design that is predicated on the principles of their optical systems. A standard system comprises a xenon lamp light source, an excitation monochromator, a quartz flow cell, an emission monochromator, and a photomultiplier tube (PMT) detector.[6–9] The design is both large and costly, and improvements can be made in the following ways: (1) by using a laser diode instead of a xenon lamp, thus reducing the size and increasing the light intensity; (2) by using a silicon photomultiplier instead of a PMT, albeit with the caveat that it has lower sensitivity and poorer linearity; and (3) by designing a flow cell with a special structure to realise the integration of the optical path and avoid the use of lenses. In summary, the combination of laser diode and silicon phototransistor can significantly reduce the size of the detector, and the optimized flow cell design is crucial for component integration.

In recent years, the rapid advancement of 3D printing technology has led to widespread application across various aspects of daily life, education, and research. When integrated with computer-aided design (CAD), 3D printing enables the creation of highly customized models, allowing the fabrication of complex structures that were previously only conceptual.[10–13] A notable example is the development of a "three-in-one" detector for capillary electrophoresis using 3D printing technology, demonstrating this approach's potential. The inherent flexibility in design, cost-effectiveness, and customizable production capabilities of 3D printing make it an ideal tool for rapid prototyping.[14] In another work, researchers have engineered a 3D-printed chemiluminescence smartphone detector for HPLC. All optical components of this detector were fabricated *via* 3D printing technology, yielding a portable, cost-effective, and user-friendly device. This innovation was successfully

---

Bio-Analytical Laboratory, Shantou University Medical College, Shantou 515041, China. E-mail: hjluosumc@stu.edu.cn; ksyuan@stu.edu.cn

† Electronic supplementary information (ESI) available. See DOI: https://doi.org/10.1039/d5ra03108g

applied to the detection of carbamazepine, demonstrating its utility in analytical chemistry.[15] Our group recently employed the 3D metal printing technique to fabricate a UV-detector that could be directly coupled to the open column chromatography, which aimed at monitoring the fraction. By using the 3D-metal printing, such detector can work effectively even in low-polarity organic solvents, and characterized by low cost and small size.[16] Therefore, using the 3D printing technique for fabricating a low-cost and miniature fluorescence detector, especially for building the flow cell, is a promising way to miniaturize the device to satisfy the above requirements.

In this work, we have designed a simple fluorescence detector for HPLC by integrating the excitation monochromator, emission monochromator, sample chamber, and detector into a compact 3D printing flow cell. Utilizing 3D printing technology, which offers a precision range of 0.1 mm to 0.5 mm, the flow cell is fabricated through layer-by-layer deposition of melted material extruded *via* a fine nozzle. This approach allows for the personalized fabrication of components tailored to specific experimental requirements. To minimize interference from scattered light, black printing material is employed to reduce the generation of scattered light, ensuring that the fluorescence detector with lower blackground noise. Additionally, integrating a voltmeter as a detector reduces the impact of stray light during emission measurements, resulting in a compact and portable integrated sample detection flow cell. Through a series of experiments, the performance of the 3D-printed fluorescence detector is rigorously evaluated to determine whether it meets the fundamental standards required for reliable fluorescence detection.

2. Results and discussion

2.1 Design and appearance of 3D printing fluorescence detector

The main component of the 3D-printing fluorescence detector is fabricated from polylactic acid (PLA) using a 3D printer, which consists of a large hollow cylinder, a small hollow cylinder, and a rectangular section designed with a light-through port and a flow cell (Fig. 1A(a)). As depicted in Fig. 1A(b), the outlet port at the terminal end of the HPLC-UV detector is connected to the large cylinder of the detector *via* a fitting screw (c′ in this image). The internal cross-section of the rectangular section is illustrated in Fig. 1B. The flow cell is constructed as a $3 \times 3 \times 3$ mm^3 chamber, with two quartz glass discs (each 7.25 mm in diameter and 1.4 mm in thickness) embedded on the left and right sides, as shown in Fig. 1A(b(b′ and d′)). Taking a closer look at the detection window of the flow cell (Fig. 1B), we find it serves two key functions: ensuring unobstructed laser transmission and enabling optical path direction adjustment for alignment. By integrating this design with the high-intensity, tightly focused characteristics of the laser beam, we eliminate the need for optical fiber and focusing lenses—simply fixing the flow cell and laser source onto an acrylic plate. This approach endows the detector with a compact structure. The design of our flow cell also allows fluorescence collection at a 90-degree angle to the direction of the incident light. More importantly, the tailor-made small-size long-pass filters and silicon photodiodes can be easily embedded to the flow cell, which further endows the detector with a compact structure. Here we use a silicon photodiode to converts the light signals into electrical signals, which are then collected by a high-precision voltmeter and recorded by the computer.

While adjusting the optical path to ensure the effective detection, the flow cell is firstly filled with mobile phase and the laser be activated, the laser beam is observed from the side that fluorescence is collected to confirm whether the laser beam forms a complete and unobstructed path through the flow cell. This step ensures that the laser fully traverses the flow cell with minimal scattering, which is critical for minimizing the detector's signal noise. If more stray light or incomplete beam is observed, the alignment is adjusted until the laser passes uniformly through the flow cell. To this end, the laser position (light direction) is finely adjusted until the stray light is at its minimum, then both the laser and the detector are stabilized in their positions. Once stabilized, the detection process can commence. The laser used in the 3D-printing fluorescence detector can be replaced according to specific experimental requirements. In this study, we focus on detecting fluorescent dyes such as rhodamine B, which can be excited by the green laser diode (central wavelength: 532 nm).

2.2 Stability of the laser diode and photoelectric conversion module

The 3D-printing fluorescence detector comprises a laser diode, a flow cell, a silicon phototube and a voltmeter. The primary objective of this experiment is to ascertain the stability of the light intensity of the laser diode, and to determine whether the detector, comprising the silicon phototube and the voltmeter, can stably receive the optical signal and convert it into a consistent electrical signal. To this end, the silicon photodiode is connected to the voltmeter, with each connector fixed with insulating tape. The silicon photodiode is then fixed at a certain height to ensure that it can stably transmit the light signal. It should be note that when the laser is directly irradiated, the silicon photodiode will inevitably sustain a certain degree of damage. Furthermore, if the measurement is conducted beyond this range, the accuracy of the results will be compromised. To mitigate the impact of the laser on the silicon photodiode, it is essential to connect the laser to a meter-long fiber optic cable, thereby attenuating the laser energy to a certain extent. The specifics are delineated in Fig. 2A(a). Next, a 60 minute short-term study is conducted. The laser is then directed towards the silicon photodiode, which is connected to the optical fiber, at 10 minute intervals to record the voltage. The specific data, as outlined in Table S1,† provides a comprehensive overview of the voltage change trend, as depicted in Fig. 2B. When the optical fiber is connected directly to the silicon photodiode, the voltage declines gradually over time. The voltage exhibited a gradual stabilization over the 60 minute period, with an average value of 0.3281, an average change in voltage of 0.0048 V per 10 minutes, an overall standard deviation of 0.0095, and an RSD of 2.89%. The stability of the laser

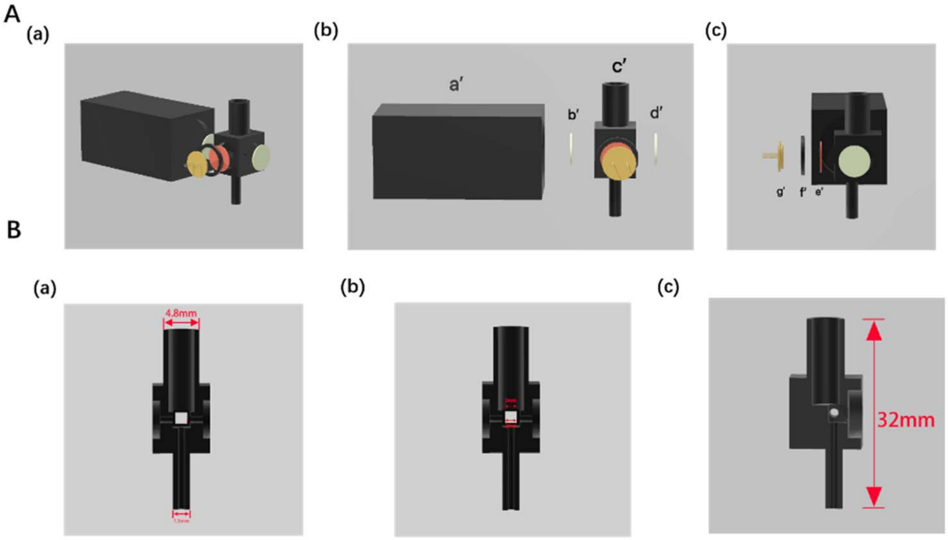

Fig. 1 Schematic illustration of the 3D printing fluorescence detector. (A) (a) is a schematic diagram of the overall device of the 3D printing fluorescence detector, (b) front view of the 3D printing fluorescence detector, (a′) is the laser, (b′) and (d′) are the quartz slides, (c′) is flow cell, (c) the 3D printing fluorescence detector inside view, (e′) is the optical filter, (f′) is the 3D printing silicon photodiode snap, and (g′) is the silicon photodiode. (B) is a schematic diagram of the cross-sectional details of the main unit of the 3D-printing UV detector, (a) and (b) are front and back views, (c) is the side view.

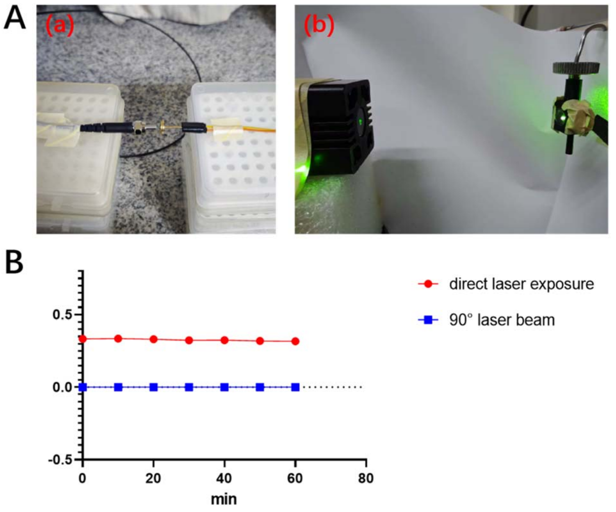

Fig. 2 (A) (a) The laser is connected to the optical fiber and then directly irradiates the silicon phototube (b) schematic diagram of the silicon phototube receiving the emitted light at 90° to the excitation light. (B) Continuous irradiation of the laser for 60 min with continuous voltage changes at different angles.

was examined after the pre-laser was lit for half an hour, and the overall average voltage of the voltage after half an hour was calculated to be 0.3215 V, with an overall standard deviation of 0.0037 and an RSD of 1.15%. After a duration of 30 minutes, the RSD of the voltage after 30 minutes was found to be lower than the RSD of the overall voltage. This finding suggests that the laser energy is more stable after 30 minutes. Consequently, prior to employing the laser, it is advisable to initiate a 30 minute warm-up period and to await the stabilization of the power supply before conducting the experiment.

The silicon photoelectric tube is positioned at the pass-through port, which is angled 90° relative to the laser intake. The 3D printing fluorescence detector is filled with liquid during operation, and the liquid is continuously replenished within the flow cell. Consequently, filling the flow cell with liquid and replenishing the liquid to simulate the operational state of the 3D printing fluorescence detector. After illuminating the laser, fixing the silicon photoelectric tube at the pass-through port and connecting the meter, the process is initiated. To ensure that the meter can receive the signal, the voltage change should be recorded over a period of 60 minutes, as illustrated in Fig. 2A(b). As demonstrated in Fig. 2B, the voltage remains stable at 0 within a 60 minute period, with an average value of 0 and no fluctuations observed. This outcome serves to verify the effectiveness of the 3D printing fluorescence detector, which is stabilized by the silicon photocell receiving voltage, provided that the assembly process is executed correctly. Consequently, it can be concluded that the correct connection of the silicon phototube, after the preheating of the laser for a duration of 30 minutes, can stabilize the 3D printing detector in its entirety, thereby minimising fluctuations and ensuring the attainment of stable and accurate experimental results.

2.3 Effect of cap of the silicon phototransistor

The silicon photodiode transforms the light signal into electric signal in the 3D-printing fluorescence detector, and its sensitivity significantly influences the detection outcomes. The silicon photodiode primarily comprises a metal shell enclosure and a blue-violet light-sensitive chip with an area of 3 mm × 3 mm. The metal casing of the silicon phototransistor has a top thickness of approximately 5 mm, which partially affects its response to light. To explore whether the sensitivity of the silicon phototransistor could be enhanced, a preliminary test was conducted under consistent light intensity and incident angle conditions by removing the top portion of the metal casing. The silicon phototransistor before and after removing the top metal casing are illustrated in Fig. 3A. Experiments were conducted using a 50 μg per mL solution of rhodamine B to evaluate the performance of the silicon phototransistor with and without the top metal encapsulation cap. The specific data are presented in Table S2,† and the trend comparison is illustrated in Fig. 3B. For the silicon phototransistor with the top metal encapsulation cap intact, the peak areas obtained from four replicate experiments were 51.15, 52.47, 47.80, and 46.58, yielding an average peak area of 49.50 and a relative standard deviation (RSD) of 5.59%. In contrast, after removing the top metal encapsulation cap, the peak areas from four replicate tests were 72.54, 72.64, 74.90, and 73.05, resulting in an average peak area of 73.28 and an RSD of 1.50%.

Above experimental results demonstrate that the peak areas obtained after removing the top metal encapsulation cap are significantly higher than those obtained with the cap intact, indicating improved sensitivity of the silicon phototransistor. Additionally, the lower RSD value after removal suggests enhanced stability of the 3D-printing fluorescence detector. Therefore, removing the silicon phototransistor's top metal encapsulation cap increases sensitivity and improves the detector's overall stability, leading to better performance. Based on these findings, the silicon phototransistor with the top metal encapsulation cap removed will be used in subsequent experiments to ensure optimal detection accuracy and reliability.

2.4 Optimization of the detection window in flow cell

The different designs of the detection window would influence on the analytical performance of the detector. In the context of our as-fabricated 3D-printing fluorescence detector, the following two main aspects in the detection window can be optimized: (a) the distance between the laser incidence port and the fluorescence receiving port (silicon phototransistor); (b) the size of the fluorescence receiving port. By optimizing these two factors, it is possible to further reduce the baseline noise level, thereby improving the detector's analytical performance.

To investigate whether the distance between the laser input port and the fluorescence receiving port affects the light intensity received by the silicon phototransistor, experiments were conducted by adjusting the internal structure of the flow cell. The interior of the flow cell constitutes a 3 × 3 × 3 mm^3 cubic space, and the position of the laser incidence port on this spatial cube was systematically modified. Two distinct versions of the flow cell model were developed, in which the distance between the laser incidence port and the fluorescence receiving port was set to 0.75 mm (model 5) or 1.5 mm (model 6). The internal structures of these two models are illustrated in Fig. 4A, along with the corresponding five replicate experiments were performed for each model under identical experimental conditions and using the same analytical solution. The voltage variations collected during these experiments were plotted. The graphs demonstrate that the voltage changes over time, indicating a correlation between the voltage fluctuations and the analyte concentration within the flow cell. For model 5, as depicted in Fig. 4A(a), the baseline values for the five experiments were 0.058, 0.061, 0.057, 0.057, and 0.056, yielding an average baseline of 0.0578. After accounting for the baseline effect, the peak areas under the curves were calculated as 61.50, 55.96, 56.54, 55.72, and 60.74, with an average peak area of 58.09. In contrast, for model 6, as shown in Fig. 4A(b), the baseline values started from zero, and the peak areas under the curves were 75.79, 76.29, 74.92, 69.39, and 67.08, resulting in an average peak area of 72.69. Considered the lower baseline values and greater peak area, model 6 has been chosen for designing the flow cell.

Next, the influence of different fluorescence receiving ports were determined, as illustrated in Fig. 4B. The 50 μg mL^{-1} of rhodamine B employed in the preceding experiments was utilized for the present experiments, and five parallel experiments were conducted for each model. As illustrated in Table S3,† the peak areas formed by the model with a 2 mm side length were 73.32, 76.79, 74.95, 75.26, and 74.79, with an average peak area of 75.02 and an RSD of 1.65%. In contrast, the peak areas formed by the model with a 3 mm vent were 72.61, 72.06, 70.70, 69.99, and 70.83, with an average peak area of 71.24. The peak area formed by the model with a 4 mm side length was 61.9, 69.57, 68.13, 71.19, 74.02, and the average peak area was 68.96, with an RSD of 6.54%. The following conclusion was drawn from the comparison of the three sets of data illustrated in Fig. 4B(d), the 3 mm and 4 mm passages exhibited no greater sensitivity than the 2 mm passages in terms of received light signals, and the RSD value of the 3 mm was equivalent to that of the 2 mm. In contrast, the RSD of the 4 mm was considerably higher than that of the 2 mm. Consequently, the 2 mm exhibited comparatively higher sensitivity and stability. Given these considerations of sensitivity and stability, 2 mm was selected.

2.5 Analytical performance of 3D printing fluorescence detector

Based on the comprehensive experimental results, we selected model 6, equipped with a 2 mm fluorescence receiving port. The silicon phototransistor was removed from the upper surface of the metal encapsulation cover to facilitate the assembly of the finalized version of the 3D-printing fluorescence detector. After

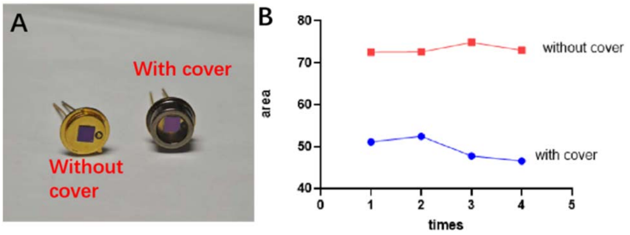

Fig. 3 (A) Real image of the silicon phototransistors before and after removing the top of the metal encapsulated case, (B) corresponding peak area of rhodamine B before and after removing the top of the metal encapsulated case for silicon phototransistors.

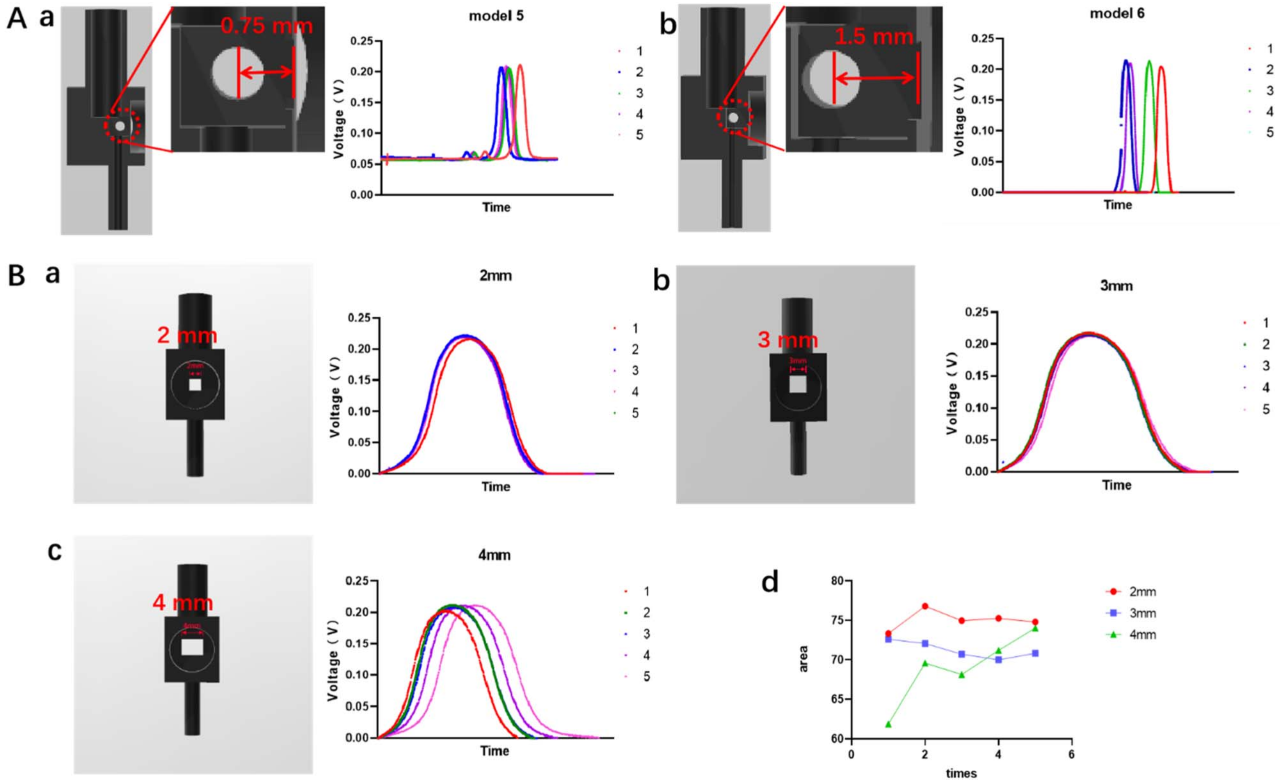

Fig. 4 Optimization of the detection window, (A) (a) is the internal detail of model 5 and corresponding peak pattern formed by five injections, (b) is the internal detail of model 6 and corresponding peak pattern formed by five injections; (B) the fluorescence receiving port with square shape and different side length of 2 mm (a), 3 mm (b), and 4 mm (c), and corresponding peak patterns formed by five injections, respectively, (d) is comparison of five parallel data from 2 mm, 3 mm, and 4 mm fluorescence receiving port.

determining the detector configuration, it was essential to evaluate the overall stability, LOD, and linear detection range of the 3D-printing fluorescence detector. Initially, we integrated the data from the HPLC UV detector and subsequently conducted experiments to determine the LOD and the linearity of the 3D-printing fluorescence detector.

A series of rhodamine B solutions with concentrations of 1 μg mL^{-1}, 5 μg mL^{-1}, 10 μg mL^{-1}, 30 μg mL^{-1}, 50 μg mL^{-1}, 60 μg mL^{-1}, and 70 μg mL^{-1} were prepared to conduct the determination. The fluorescence detector was assembled at the liquid outlet of a HPLC-UV detector. The experimental results show that the rhodamine B at 5 μg mL^{-1} can stably be detected, while 1 μg mL^{-1} cannot ensure the effective detection in every test. Therefore, we set 5 μg mL^{-1} as the LOD. It should be noted that the background noise here is 0, so we did not use the traditional 3× signal-to-noise ratio method to calculate the LOD. Possible reasons are as follows: (1) compared with ultraviolet detectors, fluorescence detectors inherently have lower background noise;[17] (2) although the silicon phototube we used has advantages such as small volume and low cost, its linear response sensitivity to optical signals is worse than that of traditional photomultiplier tubes, making it unable to detect slight fluctuations in optical signals in the system; (3) the voltage meter has limited precision. Detailed experimental results are presented in Table 1. The HPLC-UV assay data for concentrations ranging from 5 μg mL^{-1} to 70 μg mL^{-1} were fitted and analysed, yielding a linear regression equation of $Y = 15\,810X + 6715$, with R^2 value of 0.9997. Subsequently, fluorescence intensity data from the 3D-printing detector were collected, and the peak areas for concentrations between 5 μg mL^{-1} and 70 μg mL^{-1} were integrated using GraphPad Prism. The integrated peak area and concentration relationship were initially fitted to a linear equation of $Y = 0.8552X + 1.074$, with an R^2 value of 0.9767. Since $R^2 < 0.99$, the selected concentration range included values outside the linear detection range. The 70 μg mL^{-1} data point, which fell outside the linear range, was excluded to address this. The revised linear regression analysis yielded an improved $Y = 0.9421X - 0.5854$, with an R^2 value of 0.9937. This $R^2 > 0.99$ confirms that the adjusted concentration range (5 μg mL^{-1} to 60 μg mL^{-1}) lies within the linear detection range of the assay, ensuring reliable and accurate fluorescence intensity measurements.

Subsequently, the intra- and inter-day detection stability of the 3D-printed fluorescence detector was evaluated. This was achieved by comparing the detection of the same sample (50 μg per mL rhodamine B) on the same day and on different days. The specific experimental data can be found in Table S4.† To evaluate the intra-day stability, six consecutive parallel tests were performed within the same day, and the peak areas were 68.96, 63.42, 59.48, 65.92, 66.00, and 67.67, respectively, with the corresponding relative standard deviations (RSD) of 5.19%.

Table 1 Analytical performance of the detectors

Analyte	Methodology	Line	Equation	R^2
Rhodamine B	HPLC	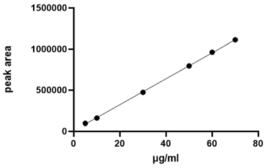	$Y = 15\,810X + 6715$	0.9997
	FD	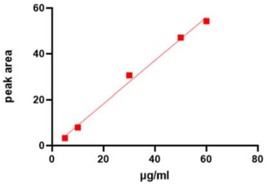	$Y = 0.9421X - 0.5854$	0.9937

Next, the same analyte (50 μg per mL rhodamine B) was analysed for five consecutive days, with three parallel experiments performed each day. The peak areas obtained were 74.95, 75.26, 74.79, 72.54, 72.64, 73.05, 75.79, 76.29, 74.92, 68.97, 66.34, 67.69, 73.36, 73.87, and 72.65, respectively, and the RSD is calculated as 4.09%.

2.6 3D printing fluorescence detector coupled with HPLC for simulating real separation and detection of mixture

This 3D printing fluorescence detector was then coupled with the PR-HPLC system to separate and detect the mixture of rhodamine 6G and rhodamine B (25 μg mL^{-1}, respectively). As demonstrated in Fig. 5A, the 3D-printing fluorescence detector produced a distinct spectrum. Similarly, Fig. 5B shows that the HPLC-UV method yielded a unique spectrum. A comparison of these spectra reveals two separate peaks, with peak shapes and elution times that are essentially identical. When both spectra are combined with the peak appearance time of a single compound under the same chromatographic conditions and after the effect of solvent peaks have been excluded, it can be determined that the first peak is the rhodamine 6G, while the second peak is rhodamine B. This experiment demonstrates the capability of the 3D-printing fluorescence detector in connecting the HPLC for analytical mixture separation and detection.

In order to ascertain whether the complex matrix would have an effect on the assay, a paprika infusion was prepared using water, and subsequently employed to dissolve rhodamine B. The results of the experiments are demonstrated in Fig. 5C and D. In the absence of any additive components, the presence of chili pepper water alone resulted in no observable response. Conversely, when rhodamine B was utilised as an additive, a discernible peak emerged within the solution, exhibiting a complete peak shape. This finding indicates that complex matrices do not influence the performance of the detector.

2.7 Integration of the 3D printing fluorescence detector

It should be noted that all the above data and chromatogram is recorded by using the 3D printing fluorescence detector in which all the components are not integrated into one unit (as depicted in Fig. 6A). And as a prototype, we have fully proved the feasibility of our idea.

Next, we try to integrate all the elements into one unit as depicted in Fig. 6B (top), along with the Fig. 6B (down) show the corresponding HPLC chromatogram of rhodamine B (50 μg mL^{-1}) recorded by such integrated device and exhibited a high degree of similarity to those detected by the device before integration. However, it should be noted that the sensitivity of the former was found to be inferior to that of the latter. Fig. 6C show real image of the 3D-printing fluorescence detector after all the components are encapsulated into a 3D printing black box.

Such integrated device also could be encapsulated into a 3D printing black box easily with very small size (39 × 79 × 40 mm). However, further refinement and improvement is required of the integrated 3D-printing fluorescence detector device. For instance, the integrated 3D-printing fluorescence detector has been found to exhibit baseline interference, which

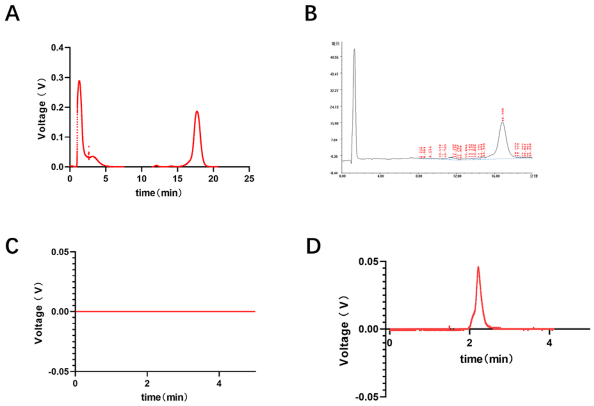

Fig. 5 Simultaneously recorded HPLC chromatograms of rhodamine 6G and rhodamine B obtained using a self − fabricated 3D-printed fluorescence detector (A) and a commercial ultraviolet (UV) detector (B). Detection of complex matrix samples of blank chili powder extraction (C) as well as rhodamine B mixed with chili powder extraction (D).

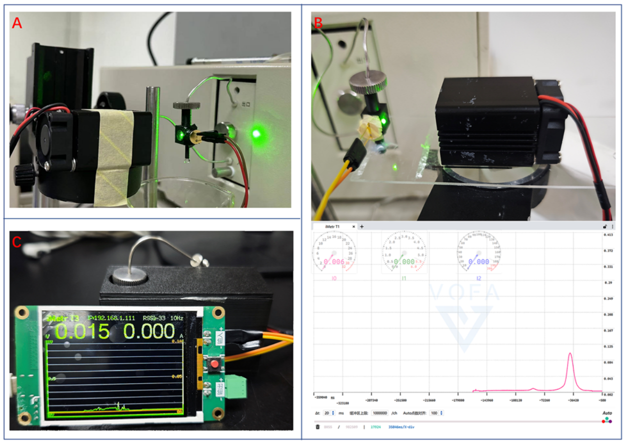

Fig. 6 (A) Real image of the 3D-printing fluorescence detector connected to the HPLC system before all the components are integrated into one unit (the prototype device), (B) real image of the 3D-printing fluorescence detector connected to the HPLC system after integrating all the components are integrated to an acrylic sheet (top) and corresponding HPLC chromatogram (down), (C) real image of the 3D-printing fluorescence detector after all the components are encapsulated into a 3D printing black box (39 × 79 × 40 mm cm).

precludes the possibility of zeroing it. A thorough analysis and hypothesis formulation have been conducted to identify the baseline and sensitivity issues, including the reduction of the distance between the flow cell and the laser, leading to enhanced internal light refraction, and the necessity for enhancing the internal structure of the flow cell to mitigate light refraction and other concerns. In summary, while the integrated 3D-printing fluorescence detector can be used without issue, there is still scope for enhancement, and further optimisation is required.

3. Conclusions

We developed a simple, portable fluorescence detector utilizing 3D printing technology for HPLC separation. The detector comprises a laser, 3D-printing flow cell, quartz glass, filter, silicon phototube, and voltmeter, and its design offers straightforward assembly, operation, and installation. Using 3D printing technology in detector construction ensures cost-effectiveness, making it a viable option for various research applications. The study examined the relationship between the distance between the flow cell's 0.75 mm and 1.5 mm fluorescence ports and the performance of the 3D-printing fluorescence detector. It was determined that a distance of 0.75 mm maintained the lower baseline. Subsequent analysis compared the fluorescence receiving port with side length of 2 mm, 3 mm, and 4 mm, determining that the 3D printing fluorescence detector exhibited optimal stability when the 2 mm was selected. Additionally, it was found that the removal of cap of the silicon phototube can improve performance of the 3D-printing fluorescence detection.

Following the determination of each component of the detector, the LOD was determined to be 5 μg mL^{-1}, the linear range was 5–60 μg mL^{-1}, and the fitted linear equation was determined to be $Y = 0.9421X - 0.5854$, ($R^2 > 0.99$). The RSD of its inter- and intra-day stability was less than 5%, which indicates that the detector meets the requirements and can also perform separation detection for the same type of mixture. This 3D-printing fluorescence detector, although not as sensitive as the general fluorescence spectrophotometer, has advantages of small size, portability, and free and flexible assembly. It is acknowledged that this 3D-printing fluorescence detector has many areas for further improvement and refinement and that there is still room for exploration and development in the future.

4. Experimental

4.1 Reagents and equipment

4.1.1 Reagents. Methanol, 99%, HPLC grade (Shanghai McLean Biochemical Technology Co., Ltd), rhodamine B, ≥99%, HPLC grade (Shanghai McLean Biochemical Technology Co., Ltd), rhodamine 6G (Shanghai McLean Biochemical Technology Co., Ltd); the water used for the experiments was ultrapure.

4.1.2 Equipment. High-Performance Liquid Chromatograph system (Dalian Jiang Shen Separation Science and Technology Company) and a 3D printer (Shenzhen Top Bamboo Technology Co., Ltd).

4.2 Experimental methods and results

4.2.1 Examining the stability of each part of the 3D-printing fluorescence detector. A silicon photodiode was fixed and connected to the laser to evaluate the stability of the laser emission over a short period and to determine the maximum detectable limit of the laser and the upper detection limit of the fluorescence detector. The laser was directly irradiated onto the silicon photodiode, and the voltage changes were monitored over 60 minutes, with data recorded at 10 minute intervals. The 3D-printing fluorescence detector was fully assembled, ensuring the flow cell was filled with the mobile phase and free from internal stray light. A laser beam was directed through the flow cell to verify whether the excitation light fully passed through the through-hole and whether the transmitted light was received at a 90-degree port. The detector was then connected, and the silicon photodiode was fixed to the receiving port of the flow cell. The laser was activated, and voltage changes were observed over 60 minutes, with data recorded at 10 minute intervals.

4.2.2 Effect of the top of the silicon photodiode metal package cover on sensitivity. A 50 μg per mL rhodamine B solution was employed as the test sample to investigate whether removing the metal encapsulation cap from the silicon photodiode would affect its optical sensitivity. The same flow cell was used for this evaluation. The 3D-printing fluorescence detector was connected to the outlet of a high-performance liquid chromatography (HPLC) system equipped with a UV spectrophotometer. The experimental conditions for the HPLC were set as: mobile phase—60% methanol solution; flow rate—0.8 mL min^{-1}; and UV detector wavelength—550 nm.

4.2.3 Detection of the effect of different 3D printing fluorescence detector flow cells on the detector

(1) The effect of the distance from the fluence port of the laser injection to the fluence port of the absorbed light of the silicon phototube. Preparation of rhodamine B solution (50 μg mL^{-1}): to prepare a rhodamine B solution with a concentration of 50 μg mL^{-1}, 0.01007 g of rhodamine B powder was accurately weighed and dissolved in 2 mL of ultrapure water to obtain a stock solution with a 5 mg per mL concentration. Subsequently, 1 mL, 0.5 mL, and 0.25 mL aliquots were taken from the stock solution and transferred into separate 50 mL volumetric flasks. Each flask was then diluted to the 50 mL mark with ultrapure water, resulting in rhodamine B solutions with 100 μg per mL concentrations, 50 μg mL^{-1}, and 25 μg mL^{-1}, respectively.

A 10 mL aliquot of a 25 μg per mL rhodamine B solution was transferred into a 50 mL volumetric flask and diluted to the mark with an appropriate solvent to yield a 5 μg per mL rhodamine B solution. Subsequently, a 10 mL aliquot of the 5 μg per mL rhodamine B solution was transferred into another 50 mL volumetric flask and diluted to the mark to obtain a 1 μg per mL rhodamine B solution. The intermediate concentration of 50 μg per mL rhodamine B solution was utilized as the test solution, and its properties were analyzed to evaluate the performance characteristics of the flow cell.

The internal configuration of the flow cell was modified to alter the distance between the through-hole and the light absorption port. The baseline and peak profiles generated by model 5 and model 6 were compared to assessing the impact of varying the distance between the through-hole and the light absorption port on the signal-to-noise ratio. This comparative analysis aimed to elucidate the relationship between the spatial configuration of the flow cell components and the resultant signal noise.

(2) Influence of the size of the absorbing optical port of a silicon photodiode on the sensitivity of light absorption. A 50 μg per mL rhodamine B solution was employed as the detection solution to systematically investigate the relationship between the absorption port's dimensions and the detection system's sensitivity and stability. The excitation light emitted by the sample at the absorption port of the flow cell was captured by a silicon phototube, which subsequently converted the optical signal into an electrical signal. The size of the absorption port directly influenced the magnitude of the optical signal detected by the phototube.

To explore this relationship, the width of the circulation absorption light port was modified using Blender software, and the redesigned components were fabricated using a 3D printer. The light transmittance was enhanced by systematically varying the width of the absorption light port in the circulation cell. The resulting optical signal was converted into an electrical signal *via* the silicon phototube, and the impact on light absorption sensitivity was evaluated by monitoring changes in the phototube's output voltage. This approach allowed for a quantitative assessment of how alterations in the absorption port dimensions influenced the system's sensitivity and stability.

4.2.4 Examining the overall performance of 3D printing fluorescence detectors. Rhodamine B solutions were prepared at concentrations of 1 μg mL^{-1}, 5 μg mL^{-1}, 10 μg mL^{-1}, 30 μg mL^{-1}, 50 μg mL^{-1}, 60 μg mL^{-1}, and 70 μg mL^{-1}. A 109 μg per mL stock solution was prepared by dissolving 0.0109 g of rhodamine B powder in 100 mL of deionized water. Aliquots of 32.11 mL, 27.5 mL, 22.9 mL, 13.75 mL, and 4.58 mL of the stock solution were transferred into separate 50 mL volumetric flasks. Each flask was diluted to the mark with deionized water to obtain 70 μg mL^{-1}, 60 μg mL^{-1}, 50 μg mL^{-1}, 30 μg mL^{-1}, and 5 μg per mL solutions, respectively. Additionally, 10 mL of the 50 μg per mL solution was diluted in a 50 mL volumetric flask to prepare a 10 μg per mL solution. These solutions were utilized to evaluate the lower limit of detection, linearity, and stability of the 3D-printing fluorescence detector.

Based on the experimental results, the flow cell and silicon photodiode configurations demonstrating optimal performance were selected and integrated to assemble a fluorescence detector under optimal conditions. The rhodamine B solutions described above were employed to assess the minimum detection limit and linearity of the 3D-printing fluorescence detector. Furthermore, the overall stability of the detector was evaluated using a 50 μg per mL rhodamine B solution, with intra-day and inter-day stability tests conducted to ensure reproducibility and reliability.

(1) Regression linearity of 3D printing fluorescence detectors. To evaluate the overall stability of the 3D-printing fluorescence detector, a series of rhodamine B solutions with varying concentrations were employed as detection samples. A high-performance liquid chromatography (HPLC) system equipped with an ultraviolet (UV) detector was utilized as a reference detector for comparative analysis. The peak profiles generated by different concentrations of rhodamine B solutions were examined to assess potential differences in peak areas and to determine whether a linear correlation existed between the peak area and the analyte concentration. This comparative study aimed to validate the performance of the 3D-printing fluorescence detector by analyzing the consistency of peak shapes, the reproducibility of peak areas, and the linearity of the concentration–response relationship.

(2) Intraday stability. To assess the intra-day stability of the 3D-printing fluorescence detector, six replicate experiments were conducted using the same concentration of rhodamine B solution within a day. The peak areas obtained from these parallel measurements were compared to evaluating the reproducibility and consistency of the detector's performance. This analysis aimed to determine the degree of variation in the peak area measurements under identical experimental conditions, thereby providing insights into the short-term stability and reliability of the 3D-printing fluorescence detector.

(3) Interday stability. In order to ascertain the interday stability of the 3D-printed fluorescence detector, the assay was conducted utilising the same concentration of rhodamine B solution for a period of five consecutive days, with three parallel experiments being performed on each day. Peak areas obtained from these parallel assays were then compared to assess the

repeatability and consistency of the detector performance. The objective of this analysis was to ascertain the extent of variability in the measured peak areas under identical experimental conditions, thereby providing insight into the stability and reliability of the three-dimensionally printed fluorescence detector.

4.2.5 3D printing fluorescence detector separation for real samples. A total of 0.00108 g of rhodamine B powder and 0.00092 g of rhodamine 6G powder were weighed and dissolved in 1 mL of ultrapure water. The mixtures were thoroughly homogenized using a vortex mixer to prepare stock solutions with 1080 μg per mL concentrations for rhodamine B and 920 μg mL^{-1} for rhodamine 6G. Subsequently, 100 μL of each stock solution was subjected to a tenfold dilution, resulting in 1 mL solutions with concentrations of 108 μg mL^{-1} for rhodamine B and 92 μg mL^{-1} for rhodamine 6G. This dilution step was repeated to obtain another set of solutions with the same concentrations. Finally, 500 μL of each diluted solution was combined in a 1 : 1 ratio to prepare a mixed rhodamine solution.

The HPLC conditions were as follows: mobile phase—50% methanol and 50% water (v/v); flow rate—0.8 mL min^{-1}; and detection wavelength—550 nm. These conditions were optimized to ensure adequate separation and accurate rhodamine B and 6G quantification in the mixed solution.

Data availability

Data will be made available on request.

Author contributions

Xuewan Wu: writing-original draft, writing-review and editing, conceptualization, methodology, data curation. Yanting Liu: conceptualization, methodology, writing-review and editing. Ziyi Xiao: data curation, writing-review and editing. Ruyi Deng: data curation, writing-review and editing. Rui Huang: writing-review and editing. Hongjun Luo: writing-review & editing, supervision. Kaisong Yuan: writing-review & editing, supervision, funding acquisition, conceptualization, methodology.

Conflicts of interest

The authors declare that they have no known competing financial interests or personal relationships that could have appeared to influence the work reported in this paper.

Acknowledgements

This work was funded by the National Natural Science Foundation of China (grant no. 22204095), Guangdong Basic and Applied Basic Research Foundation (grant no. 2023A1515010611, 2025A1515011553, 2023A1515140131), and SUMC Scientific Research Initiation Grant (grant no. 510858045).

Notes and references

1 S. Wang, B. Liu, D. Yuan and J. Ma, *Talanta*, 2016, **161**, 700–706.
2 A. Aghazadeh-Habashi, W. Asghar and F. Jamali, *J. Pharm. Biomed. Anal.*, 2015, **110**, 12–19.
3 Z. Zhu, M. Lies and J. Silzel, *Anal. Chim. Acta*, 2021, **1183**, 338936.
4 D. Shamsaei, S.-A. Hsieh, I. Ocaña-Rios, S. J. Ryan and J. L. Anderson, *Anal. Chim. Acta*, 2023, **1280**, 341863.
5 K. Zamuruyev, M. S. F. Santos, M. F. Mora, E. A. Kurfman, A. C. Noell and P. A. Willis, *Anal. Chem.*, 2021, **93**, 9647–9655.
6 Y. Tripathi, High Pressure Liquid Chromatography, in *Cellular and Biochemical Science*, 2010, ch. 55, pp. 1271–1309.
7 X.-X. Fang, H.-Y. Li, P. Fang, J.-Z. Pan and Q. Fang, *Talanta*, 2016, **150**, 135–141.
8 D. C. Mukunda, V. K. Joshi and K. K. Mahato, *Appl. Spectrosc. Rev.*, 2020, **57**, 1–38.
9 J. R. Lakowicz, in *Principles of Fluorescence Spectroscopy*, ed. J. R. Lakowicz, Springer US, Boston, MA, 1999, pp. 25–61, DOI: 10.1007/978-1-4757-3061-6_2.
10 E. J. Carrasco-Correa, D. J. Cocovi-Solberg, J. M. Herrero-Martínez, E. F. Simó-Alfonso and M. Miró, *Anal. Chim. Acta*, 2020, **1111**, 40–48.
11 L. Yang, G. Pan, P. Zhang, Q. Liu, X. Liu, Y. Li, Y. Liang and M. Zhang, *Anal. Chim. Acta*, 2021, **1159**, 338427.
12 A. S. Malinick, C. P. Ebel, D. D. Stuart, S. N. Valiulis, V. A. Hanson and Q. Cheng, *Front. Anal. Sci.*, 2024, **4**, 1505510.
13 E. J. Carrasco-Correa, E. F. Simó-Alfonso, J. M. Herrero-Martínez and M. Miró, *TrAC, Trends Anal. Chem.*, 2021, **136**, 116177.
14 Y. Wang, Z. Zeng, L. Yang, H. Zeng, Y. Li, Q. Pu and M. Zhang, *Anal. Chem.*, 2023, **95**, 2146–2151.
15 D. Shamsaei, S.-A. Hsieh, S. J. Ryan and J. L. Anderson, *Talanta*, 2025, **284**, 127156.
16 Y. Liu, X. Li, H. Luo, R. Huang, X. Wu, L. Tan, J. Guo and K. Yuan, *J. Chromatogr. A*, 2025, **1749**, 465884.
17 C. A. Farthing, D. E. Farthing, S. Koka, T. Larus, I. Fakhry, L. Xi, R. C. Kukreja, D. Sica and T. W. B. Gehr, *J. Chromatogr. B*, 2010, **878**, 2891–2895.